



Cite this: *J. Anal. At. Spectrom.*, 2018, 33, 283

Towards femtosecond laser ablation ionization mass spectrometric approaches for chemical depth-profiling analysis of lead-free Sn solder bumps with minimized side-wall contributions

A. Cedeño López, *^a V. Grimaudo, ^a P. Moreno-García,^a A. Riedo, ^b M. Tulej, ^c R. Wiesendanger, ^c P. Wurz ^c and P. Broekmann^a

Received 25th August 2017
Accepted 4th January 2018

DOI: 10.1039/c7ja00295e

rsc.li/jaas

Sn solder bumps on Cu pillars and the quantification of incorporated organic impurities are of urgent interest to the microchip industry. In this report, the fundamentals of laser–matter interaction using femtosecond laser ablation ionization mass spectrometry (fs-LIMS) are described, including studies on the ablation rate of a dual layer system Sn/Cu as well as on three different laser ablation approaches that (i) address the highly different material properties of Sn and Cu and (ii) allow for a significant reduction of side-wall contributions, which is a crucial prerequisite for chemical depth profiling.

Introduction

The thriving progress in microprocessor manufacturing constantly brings along novelties in the materials science field, which facilitates the emergence of increasingly more complex and more powerful logic and memory devices. The urge for miniaturization of these devices requires their architecture to become smaller and more complex. At the same time, increasing digitalization of processes demands high-speed and high-efficiency data transport. This is why improving interconnect technology like *e.g.* flip-chip technology and solder bumping is of outstanding interest to current research and development.

A crucial innovation in solder bumped flip-chips is the use of lead-free Sn bumps deposited on Cu pillars, which serve to interconnect semiconductor devices such as integrated circuit (IC) chips and microelectromechanical systems (MEMS) to circuit boards.^{1–3} The two metallic components of the bumps are sequentially deposited on the substrate by means of an additive-assisted electrodeposition approach. Fig. 1 shows SEM images of a typical Sn–Cu bump before and after a reflow treatment (panels a and b, respectively). The fabrication of such bump features by electrochemical deposition (ECD) enables a fast, straightforward, and low-cost fabrication. However, the use of organic additives during ECD might bring along partial embedment of organic impurities inside the metal matrices.

The reliability of the resulting IC, *e.g.* lifetime of the device, strongly depends on the degree of organic contamination inside the Sn–Cu bumps. Therefore, to shed light on the chemical nature and the amount of incorporated impurities, an elaborated spatial chemical analysis of the two layers is required prior to further processing steps of the as-prepared Sn bumps.

However, the 3D chemical composition analysis of the bump arrays is challenging, as a single bump has a spatial dimension of tens of micrometres and chemical information is required with a depth resolution of tens of nanometres. Additionally, the distinct physical properties of Sn and Cu (*e.g.* hardness and electrical and thermal conductivity) restrict the choice of suitable measurement techniques.

Therefore, most of the well-established measurement techniques for high spatial resolution analysis of the chemical composition of solids may not be considered suitable for the analysis of the target experimental system. This is because their applicable range is, in many cases, rather narrow due to constraints regarding *e.g.* detection sensitivity, quantification capability, spatial resolution, and measurement time.

Among the spectroscopic approaches, transmission electron microscopy (TEM),⁴ Auger electron spectroscopy (AES),^{5,6} X-ray

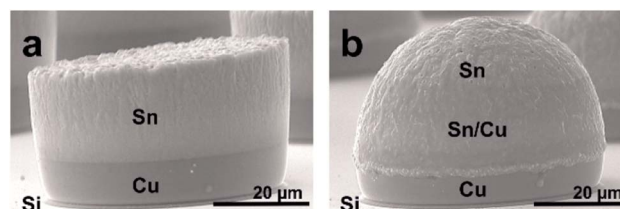


Fig. 1 Example of a Sn solder bump electrodeposited on a Cu pillar (a) before and (b) after reflow.

^aDepartment of Chemistry and Biochemistry, Interfacial Electrochemistry Group, University of Bern, Freiestrasse 3, 3012 Bern, Switzerland. E-mail: alena.cedeno@dcb.unibe.ch; Tel: +41 316314269

^bSackler Laboratory for Astrophysics, Leiden Observatory, Leiden University, Niels Bohrweg 2, 2333 CA Leiden, The Netherlands

^cPhysics Institute, Space Research and Planetary Sciences, University of Bern, Sidlerstrasse 5, 3012 Bern, Switzerland

photoelectron spectroscopy (XPS),^{7,8} and X-ray fluorescence stand out due to their powerful analysis capabilities. They provide excellent spatial resolution and information on elemental composition, but are restricted in their measurement range.⁹ Similar drawbacks hold true for atom probe tomography (APT), which provides atomic scale chemical resolution, but can only be applied on nanometre-sized specimens.^{8,10,11}

To characterize the bulk material of larger samples without preceding sample preparation steps, usually spectrometric approaches, which offer less lateral resolution, but allow for higher sensitivity detection,⁶ are applied, *e.g.* secondary ion mass spectrometry (SIMS),^{12,13} glow discharge mass spectrometry (GD-MS),¹⁴ and laser ablation inductively coupled plasma mass spectrometry (LA-ICP-MS).^{15,16} NanoSIMS is very common and widely used in industry as it offers a high spatial resolution (<50 nm). Its drawback is, however, related to quantification problems as for any direct analysis technique without perfectly matched standards. These difficulties are even more pronounced in imperfectly layered materials. Therefore, chemical quantitative bulk depth composition measurements are not possible by means of nanoSIMS.^{13,17} GD-MS and LA-ICP-MS are superior to SIMS concerning the reduction of the influence of matrix effects, measurement duration and detection sensitivity. Yet again, resolution constraints limit the analysis scope (GD-MS: mm scale lateral resolution; LA-ICP-MS: approx. 50 nm vertical resolution).¹⁵

Given the disadvantages of the techniques described above when facing demanding experimental systems like Sn–Cu bumps, novel approaches to chemical depth profiling are required. One promising alternative is depth profiling by laser ablation/ionization mass spectrometry (LIMS). As shown in previous publications,^{18–21} LIMS has the capability to provide chemical quantitative measurements of solid samples with a lateral and depth resolution in the micrometre and the nanometre range, respectively. It has a high detection sensitivity down to the tens of ppb level and, as shown recently, is capable to provide 3D chemical composition analysis of solid multi-component materials.²²

In this report, we use a reflectron-type time-of-flight (R-TOF) mass spectrometer combined with a fs-laser ablation/ionization source (instrument name: Laser Mass Spectrometer (LMS)²³), which allows quantifying the chemical (element and isotope) composition of solids with a lateral resolution of about 10–20 μm and a vertical resolution in the nanometre range.

To gain fundamental knowledge and approach the complex measurement problem, a simplified model system for the as-prepared Sn–Cu bumps consisting of electrodeposited Sn–Cu bi-layers (see Fig. 2) was investigated. These bi-layers are thinner and laterally more extended than the target Sn bumps. This makes their analysis straightforward and allows us to focus on the main challenges faced when attempting to obtain a chemical depth profile of a multi-component system with significantly different physical characteristics. For the first time, we demonstrate the extent of side-wall contributions to the quantification of depth-profiling measurements promoted by fs-laser ablation with quasi-top-hat pulse profiling using LIMS. To the best of our knowledge, this is the first dedicated report

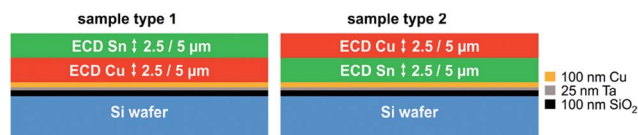


Fig. 2 Schematic of the two investigated model bi-layer samples differing in their specific layer sequence: sample type 1 (Sn–Cu) and sample type 2 (Cu–Sn). The covering Sn–Cu and Cu–Sn bi-layers are typically formed on the substrate by means of an electrochemical deposition (ECD) process on top of a Cu-seeded Si wafer coupon.

on such fundamental studies performed on these aspects for Sn–Cu bi-layers. Our motivation is to develop new measurement methodologies for depth profiling that can be transferred to the as-prepared Sn–Cu bump system.

Experimental

ECD of bi-layer samples

Bi-layer samples were prepared on blanket copper wafer coupons (Hionix Cu blanket wafer) that comprised a 100 nm thick physical vapour deposited (PVD) Cu seed layer, a 25 nm thick Ta layer, and a 100 nm TOX/SiO₂ film on a Si(100) substrate. The surface area of the wafer substrate exposed to the plating bath was 0.25 cm². A three-electrode setup was used for ECD consisting of the Cu wafer coupon as the working electrode, a Pt wire in a separate compartment as the counter electrode, and a double junction Ag/AgCl (3 M KCl) reference electrode (Metrohm Autolab B.V., the Netherlands). Two types of bi-layer samples were prepared for this study, which only differed in their particular layer sequence (see Fig. 2). For the metal plating the wafer coupons were fixed on a rotating disk electrode (RDE). Cu electrodeposition was performed under strictly static conditions whereas Sn plating was carried out under additional forced convective conditions at a given rotational speed of the RDE.

For each type of sample the two individual metal layers were varied in their thicknesses (either 2.5 or 5 μm , respectively). Galvanostatic metal deposition was carried out at a constant current density by using a commercial potentiostat/galvanostat (Metrohm Autolab B.V., the Netherlands). Detailed plating conditions for the sample preparation are listed in Table 1. The rotation of the working electrode (RDE) in the case of Sn deposition was achieved with a rotator (Pine Research Instrumentation, USA).

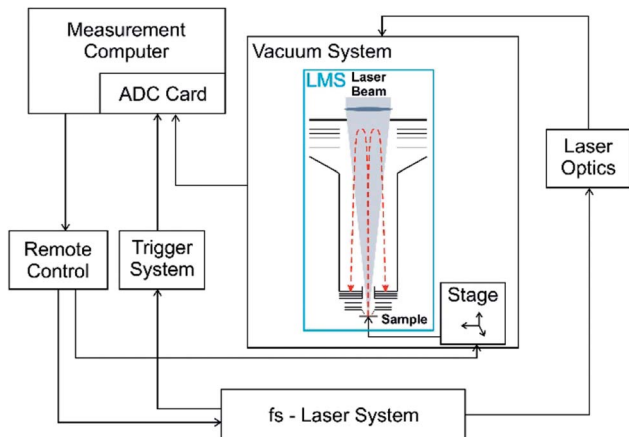
Laser ablation ionization mass spectrometry

Element analysis experiments of the bi-layer samples were carried out using the LMS instrument.^{21,23} A brief description of the instrumental setup and principle of operation is given below and is schematically represented in Fig. 3.²² More detailed technical information and the figures of merit of the instrument can be found in previous publications.^{21,24–27}

An ultra-short pulsed Ti-sapphire laser system ($\tau \sim 190$ fs, $\lambda = 775$ nm, laser pulse repetition rate ≤ 1 kHz, pulse energy ≤ 1 mJ) was used to irradiate and ionize the sample material. An

Table 1 Plating conditions for Cu and Sn electrodeposition. Metallizations were produced in two different thicknesses

| Material | Layer thickness (μm) | Plating time (s) | Current density (mA cm^{-2}) | Rotational speed (rpm) |
|----------|-----------------------------------|------------------|---|------------------------|
| Cu | 2.5/5 | 338.5/676.9 | -20 | 0 |
| Sn | 2.5/5 | 29.7/59.4 | -100 | 800 |

**Fig. 3** Schematic of the LMS instrument setup.^{21,22,24}

optical system is used to guide the laser pulses towards the mass spectrometer located in the vacuum chamber (typical base pressure at the mid 10^{-8} mbar level). In comparison to previous mass spectrometric measurements using the LMS system,^{21,24–27} a beam shaper (Focal- π Shaper 9, AdlOptica GmbH, Germany) was integrated in the beam delivery system for this current study. The beam shaper converted the Gaussian-shaped raw laser beam profile delivered by the femtosecond laser system into a quasi-top-hat beam profile. A lens system placed on top of the instrument was used to focus the laser pulses through the mass spectrometer towards the sample surface (typical spot size of $20 \mu\text{m}$ in diameter). A high-resolution x - y - z translation stage guaranteed precise positioning of the samples underneath the entrance of the mass analyser. The sample positioning was furthermore visually controlled using a new and in-house designed microscope system (micrometre resolution) situated in close proximity to the mass spectrometer.

Two 12 bit high speed digitizer PCIe cards (U5303A, Keysight Technologies, USA) providing two channels each with a maximum sampling speed of 3.2 GS s^{-1} were used to record the measured time-of-flight spectra. Custom-made software for the operation of the digitizer cards and the use of SSDs for fast data storage enabled the saving of single laser shot time-of-flight spectra on the host computer at 1 kHz frequency, the maximum repetition rate of the laser system.

A typical measurement can be run fully automated by custom-made software for the control of the laser system, the data acquisition card, and the sample positioning stage. After ablation and ionization of the sample material only positively charged species can enter the ion optical system of the LMS. The ions are accelerated, focused and confined towards the drift

path of the mass spectrometer and reflected at the ion mirror towards the multi-channel-plate detector system (chevron configuration) finally passing a second time through the drift path. The ions arrive according to their mass over charge ratio sequentially in time at the detector system (TOF principle). The recorded time-of-flight spectra are then converted into mass spectra,²¹ using in-house designed software for the conversion and analysis of detected peaks.²⁸

Crater formation study. A study on the mechanism of crater formation on sample type 1 was conducted at a laser pulse energy of $0.3 \mu\text{J}$. Between 50 and 500 laser shots were applied for the generation of craters. Experiments were repeated 5 times each for statistical significance with a $100 \mu\text{m}$ spacing between individual craters.

Study on laser pulse energy dependence. We conducted a study on the effects of increasing laser pulse energy on the ablated area and mean ablation rate on samples type 1 and 2 ($2.5 \mu\text{m Sn}/2.5 \mu\text{m Cu}$ and $2.5 \mu\text{m Cu}/2.5 \mu\text{m Sn}$, respectively). 50×10 single laser shots were applied at laser pulse energies ranging from 0.2 to $9.4 \mu\text{J}$. Experiments were repeated 3 times each for statistical significance with a crater spacing of $100 \mu\text{m}$.

Reduction of side-wall contributions

Single-step approach. The depth profiling analysis was carried out on sample type 1 ($2.5 \mu\text{m Sn}/2.5 \mu\text{m Cu}$) using one single set of laser ablation parameters ($2.5 \mu\text{J}$ pulse energy) for the entire depth profile (Fig. 9, panel a).

Multi-step approach. We developed multi-step depth profiling approaches with sets of laser ablation parameters optimized for each specific metallic component of the bi-layer system to account for their significantly different physical properties. These approaches consisted of three individual steps: a depth profiling step for Sn, a depth profiling step for the underlying Cu, and an intermediate preparation step. This intermediate preparation step was intended to selectively remove material from the topmost metal layer and reduce disturbing side-wall contributions which would otherwise originate from the topmost metal layer (e.g. Sn) while depth profiling the lower one (e.g. Cu).

Two different types of two-dimensional laser spot raster arrays were investigated and are shown in Fig. 8b and c, respectively. For step 1 (Sn depth profile analysis) in the 'rectangular' approach shown in Fig. 8b, 30 single laser shots at $0.9 \mu\text{J}$ were applied. This number of laser shots was sufficient to reach the underlying Cu layer without significant Cu removal. For step 2 (extra surface treatment) a 2D raster of laser ablation spots was applied to the surface for further Sn removal under identical ablation conditions to step 1. The raster comprised $20 \mu\text{m}$ -spaced 3×3 ablation spots. For step 3 (Cu depth profile analysis) the laser pulse energy was increased to $3.2 \mu\text{J}$. This

second depth profiling was carried out exactly at the site where the original Sn crater had been formed in step 1 and was achieved by applying 300 single laser shots. This multi-step depth profiling approach will be discussed below on the basis of Fig. 9b.

A further improvement of the multi-step depth profiling could be achieved by the optimization of the laser ablation conditions and the particular geometry of the 2D matrix of ablation spots used for the intermediate surface treatment, as shown in Fig. 8 panel c. The initial Sn depth profile (step 1) was realized by applying 60 single laser shots at 0.3 μJ pulse energy. The 2D raster in step 2 consisted of 8 spots concentrically positioned around the initial crater formed in the Sn layer during depth profiling in step 1 (60 single laser shots on each spot with a pulse energy of 0.3 μJ). This gave rise to a 'flower'-shaped appearance of the raster of ablation spots, and again, the pulse energy was too low to induce harsh ablation of Cu. The following depth profiling analysis of the Cu layer (step 3) was realized by applying 40×5 single laser shots at 3.2 μJ . This multi-step depth profiling approach will be discussed below on the basis of Fig. 9, panel c.

Note that due to the current instrumental design^{21,22,24} it was not possible to use different laser spot sizes for ablation of Sn and Cu, respectively, without impairing the reproducibility of measurements. Therefore, the campaigns were conducted with the given spot parameters.

AFM measurements

Atomic Force Microscopy (AFM) images of laser ablation craters were recorded with a FlexAFM V5+, 100 μm scan head (Nanosurf AG, Switzerland) mounted onto a FlexAFM 5 Sample Stage Pillar Kit 204 (Nanosurf AG, Switzerland) in contact mode using ContAl-G cantilevers (Innovative Solutions Bulgaria Ltd., Bulgaria). Images were recorded with a size of 75 $\mu\text{m} \times 75 \mu\text{m}$, 256 points per line and 6 s per line.

SEM and EDX measurements

Secondary electron micrographs were recorded with a Hitachi S-3000N Scanning Electron Microscope (SEM) (Hitachi, Japan) applying an accelerating voltage of 25 keV at a working distance of 10 mm. Samples were fixed on conductive adhesive tapes (Ted Pella, Redding, USA) on a metal plate.

Energy-dispersive X-ray spectroscopy (EDX) mapping was performed at an accelerating voltage of 25 keV at a working distance of 15 mm and with a resolution of 1024×768 pixel.

HR-SEM measurement

High-resolution SEM (HR-SEM) images were recorded using a field emission scanning electron microscope DSM 982 Gemini (Zeiss, Oberkochen, Germany) applying an accelerating voltage of 5 kV at a working distance of 9–11 mm. For the measurement all specimens were fixed on metal stubs with conductive adhesive tabs (Ted Pella, Redding, USA).

Results and discussion

Differences in laser–matter interactions between Sn and Cu

Sample type 1 with Sn in the upper and Cu in the lower ECD layer (see Fig. 2) directly mimics the target system, the industrially manufactured Sn–Cu bumps (see Fig. 1). To further obtain a fundamental understanding of the differences in laser–matter interactions between Sn and Cu, sample type 2 with Cu in the upper and Sn in the lower layer was also investigated. Fig. 4a and b show HR-SEM images of typical craters generated after ablating the material with the LMS instrument on samples type 1 (2.5 μm Sn/2.5 μm Cu, panel a) and type 2 (2.5 μm Cu/2.5 μm Sn, panel b) at a comparable laser pulse energy and number of applied laser shots.

A first striking difference between samples type 1 and 2, which can be observed for both low and high pulse energies, is the general appearance and distinct lateral expansion of the craters as can be seen in the HR-SEM images in Fig. 4. On sample type 1 with Sn in the upper layer the craters appear much larger than on sample type 2 with Cu in the upper layer. This is because the affected zone, a zone that is only superficially affected by the laser ablation process, is significantly more pronounced on the Sn surface than on the Cu surface.

Fig. 5 shows an AFM measurement of a typical crater formed after laser ablation on sample type 1 (2.0 μJ , 1000 laser shots). This crater seems to be made up of two different concentric depressions with characteristic diameters. The outer depression on the Sn surface spans nearly 50 μm , is of shallow depth, and is surrounded by droplet-like protrusions at its border. This region represents the above mentioned affected zone. The inner depression is the actual crater formed on the underlying Cu layer and is confined ($\sim 20 \mu\text{m}$) in width approximately to the nominal laser diameter. Its size and shape are similar to those of the actual crater observed on the Cu surface of sample type 2 (see Fig. 4b). Different laser-mediated effects on the surface material in close proximity to these actual craters on the two distinct surfaces were observed, which become noticeable in the HR-SEM images shown in Fig. 4a and b with sample type 1 on the left and sample type 2 on the right hand side. This agrees with different periodic structures observed in metals like Cu and group XIV semiconductor surfaces, which are induced by femtosecond laser ablation.²⁹ The HR-SEM image of sample type 2 furthermore reveals additional information. Here, it can

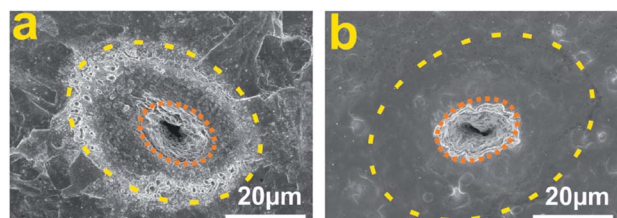


Fig. 4 SEM images recorded at the same magnification of LIMS craters on (a) samples type 1 and (b) type 2 obtained for similar laser pulse energies (2.5 μJ for sample type 1, and 2.3 μJ for sample type 2, 1000 laser shots each). The Cu crater is marked in orange and the affected zone is marked in yellow.

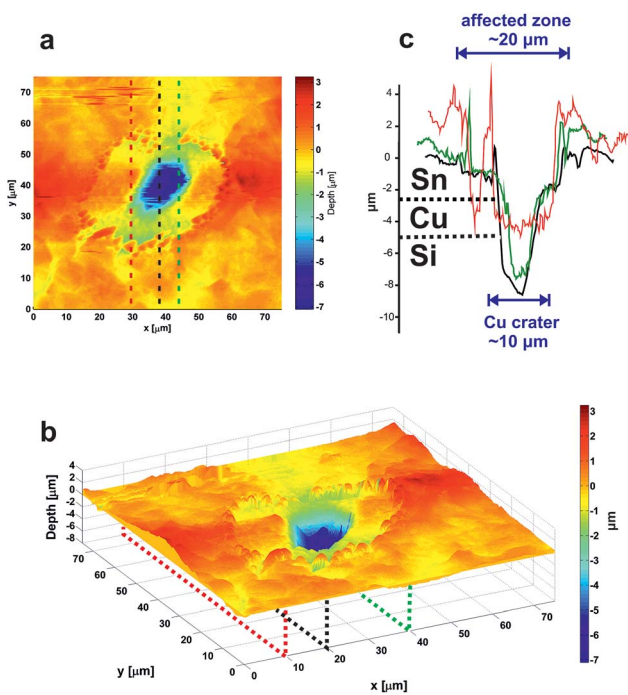


Fig. 5 (a) AFM image obtained from a typical crater on sample type 1 formed with 1000 laser shots at $2.0 \mu\text{J}$ laser pulse energy. (b) 3D representation of the crater. The dotted lines in panels (a) and (b) indicate the location of selected line scans shown in panel (c).

be recognized that the affected zone is submitted to a surface cleaning by the laser beam. The size of the affected zone is similar to that of the affected zone observed on the Sn surface layer of sample type 1. These observations indicate that the small actual crater observed on both samples type 1 and 2 arises from the interaction of the main part of the top-hat-shaped laser beam, while the affected zone can be attributed to the residual low-intensity beam wings. The appearance of beam wings is indicated in the instrument information of the beam shaper distributed by the supplier (π Shaper, AdlOptica GmbH, Germany). The dissimilar effects of these wing portions on Sn and Cu can be rationalized by the differences in the damage and ablation thresholds of the respective materials. For Cu, these thresholds are much higher than for Sn, so that mainly the most intense part of the laser beam is able to induce surface modification and ablation of the material.

The less intense wings of the beam profile only slightly affect the Cu surface. Sn on the other hand has a lower damage and ablation threshold than Cu, so that not only the main part of the laser beam, but also the wings can, to a lesser extent, induce surface modifications and even ablation of the sample material. However, ablation by the wings is less effective than ablation by the most energetic beam component, which is why in the affected zone also pronounced reflow phenomena following thermal activation occur, giving rise to droplet-like protrusions. Comparable effects are negligible on the Cu surface of sample type 2. The higher melting point (T_m) and thermal conductivity (λ) of Cu ($T_m(\text{Cu}) = 1085 \text{ }^\circ\text{C}$, $T_m(\text{Sn}) = 232 \text{ }^\circ\text{C}$; $\lambda(\text{Cu}) = 401 \text{ J s}^{-1} \text{ m}^{-1} \text{ K}^{-1}$, $\lambda(\text{Sn}) = 67 \text{ J s}^{-1} \text{ m}^{-1} \text{ K}^{-1}$)³⁰ give rise

to a lower thermal impact resulting in a less pronounced affected zone.³¹ Compared to sample type 1, significantly less melting and recrystallization are observed in the affected zone of the crater on sample type 2 where the laser beam wings interact with the Cu surface (see Fig. 4b). We also notice the presence of laser-induced periodic surface structures (LIPSS, ripples) next to the actual crater boundaries of the Cu sample, which emerge from the interference of the laser beam and a surface electromagnetic wave (SEMW) that is formed on the sample surface. This process likely goes along with the excitation of surface plasmon polaritons (SPPs).^{29,32–37} These phenomena do also occur on the Sn surface, but are less observable due to the higher degree of surface roughness resulting from more severe laser-induced reflow processes.

Crater evolution study on Sn

To investigate the evolution of the crater diameter and crater depth upon laser erosion, a study with different numbers of applied laser shots targeting sample type 1 with $5 \mu\text{m}$ thick layers at $0.3 \mu\text{J}$ fixed laser pulse energy was conducted. Because of the pronounced reflow phenomenon identical ablation crater profiles are not likely to occur, and thus several craters were evaluated for each laser energy condition and these representative samples included. We found that the diameter of the actual crater, *i.e.*, the inner depression observed on Sn, hardly changes with the number of applied laser shots (see Fig. 6). The shape of the beam profile can therefore be considered top-hat-like. As expected, the depth of the actual crater and, to a lesser extent, also that of the affected zone clearly increase with the number of applied single laser shots. Fig. 6 shows the well-known fact that the ablation rate is larger during the first pulses and gradually decreases with the pulse number. It is therefore challenging to investigate very thin layers. However, under optimized instrumental settings, studies on thin layers are possible with LIMS.^{18,19}

The pronounced occurrence of recrystallization phenomena resulting from the surface-laser interaction caused the formation of μm -scale protrusions aside the cavities formed upon material ablation. This reflects Sn-specific surface processes induced by low-energy laser irradiation. Note that if the crater aspect ratio is too large, the topology of the crater bottom can no longer fully be resolved by AFM analysis (see the black curve in Fig. 5 panel c). The surface roughness observed at the bottom of shallower craters, as shown in the orange and green curves in Fig. 5 panel c and the bottom panel of Fig. 6, is qualitatively similar over different experiments.

Differences in laser ablation behaviour on Sn and Cu

As discussed in the previous sections, laser-matter interactions between Sn and Cu clearly differ at a constant laser pulse energy ($\sim 2.3 \mu\text{J}$). The distinct ablation behaviour, *e.g.* concerning the ablated area and the mean ablation rate, becomes even more obvious in experiments where laser pulse energies are varied. Panels a and b of Fig. 7 (log/log-scale) present the dependence of the ablated area and the mean ablation rate of Sn and Cu as investigated on samples of type 1 and 2 covering a laser pulse

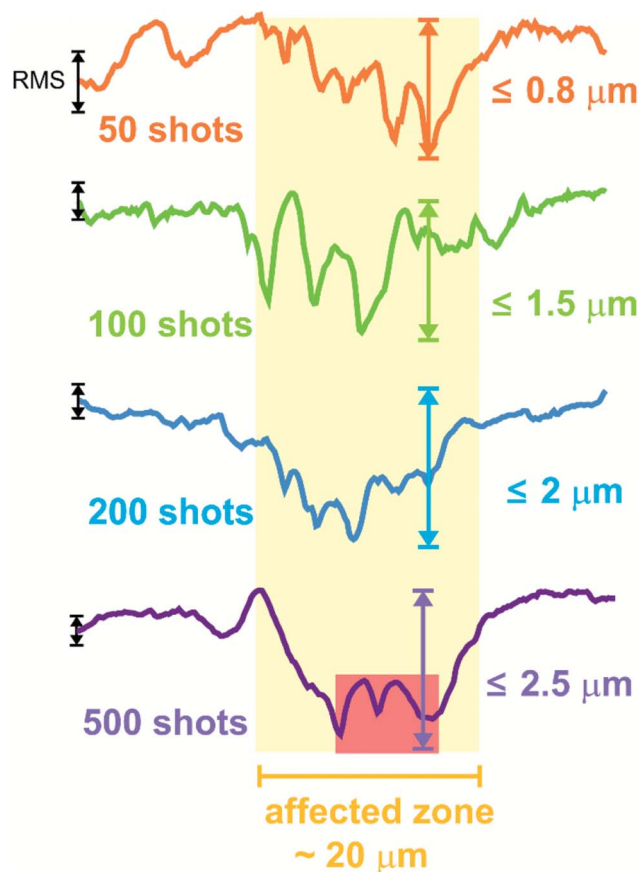


Fig. 6 AFM line scans obtained for the craters resulting from different numbers of laser shots sent to the Sn surface of the 5 μm double layer sample type 1 at 0.3 μJ . The RMS surface roughness (0.3 μm) is given with respect to the height scale on the left hand side of each line scan. The actual crater is highlighted with the pink rectangle.

energy range of 0.2–9.4 μJ . The ablated area was determined on the basis of SEM images of the craters formed on samples type 1 and 2. For sample type 1, the ablated area was considered as the entire affected zone, as also the less intense beam wings were energetic enough to induce ablation of surface Sn, whereas for sample type 2 the ablated area was considered as the actual crater, as no ablation was observable in the affected zone on sample type 2. Concerning the dependence of the ablated area on the applied laser pulse energy (Fig. 7a), we observed two distinct regimes. The relatively large ablated area on Sn in sample type 1 does not sharply rise further with increasing laser pulse energy, because at all instances the laser pulse energy exceeds the ablation threshold of the material. Therefore, the ablated area seems to reach a plateau already at slightly elevated laser pulse energies (see green data points in Fig. 7a).

Due to the significantly higher ablation threshold, actual Cu craters on sample type 2 can only be generated at higher laser pulse energies as those sufficient for ablation of Sn (compare green and red data points, full symbols, in Fig. 7a). This becomes obvious in our study, as the applied laser pulse energies are comparably low. However, at elevated laser fluences, the plasma ignition thresholds of Sn and Cu are very similar.³⁸ The weak dependence of the crater size and the increasing laser

power at elevated pulse energies are characteristic of a top-hat-like beam profile with steep crater walls. However, the stronger dependence of the laser pulse energy on the ablated area observed at low laser energies approaching the damage threshold (such as reached for Cu in Fig. 7a, cross symbols) is a result of the depth-dependence of the ablation rate (Grimaudo *et al.*, 2018, *Anal. Chem.*, in press).

The dependence of the mean ablation rate on the laser pulse energy (Fig. 7b) shows an approximately linear behaviour at laser pulse energies exceeding the ablation threshold, which again speaks for a near top-hat beam profile. The low ablation threshold of Sn allows for efficient material ablation already at relatively low pulse energies, where no ablation is observed on Cu. It was found that the data obtained for Sn and Cu in the upper layer come to lie on almost the same trend line. Note that only a specific part of the entire range of ablation rate values for both Cu and Sn is plotted in Fig. 7 as a result of the experimental design. In this experiment, the mean ablation rate was defined as the number of laser shots required to ablate a nominal layer thickness of 2.5 μm , which was considered to be the case with the onset of the underlying material signal, *i.e.*, Cu or Si, respectively.

Therefore, Cu craters formed at laser pulse energies lower than 3.0 μJ for which the Si substrate was not reached were excluded from Fig. 7. Furthermore, the layer thickness of 2.5 μm dictated the upper limit of the mean ablation rate range accessible to analysis in this campaign. Importantly, the lowest data points shown are not equivalent to the damage or ablation threshold for Sn or Cu. Sufficiently above the ablation threshold the mean ablation rate increases linearly with the pulse energy, which is illustrated by the trend line with slope = 1 in Fig. 7b.

However, if Cu is located in the lower layer like in sample type 1, Cu ablation is observed already at much lower laser pulse energies, as shown by the red cross-shaped data points in Fig. 7b. The data points for Cu in the lower layer come to lie on a trend line with a quadratic dependence (slope = 2) on the pulse energy, which is in contrast to the trend line observed for Sn and Cu in the upper layer. Most likely, quadratic dependence above an energy threshold of about 1 μJ per pulse can be attributed to laser-induced alloy formation at the interface between the upper Sn and the lower Cu layer.^{39–42} The alloy phase will display a lower damage and ablation threshold than pure Cu due to its Sn content, which might result in facilitated ablation of the alloy in contrast to pure Cu as it is found in the surface Cu layer of sample type 2 (Cu–Sn).

In earlier studies, the ablation was furthermore observed to highly depend on the surface texture.²² In this study, the discrepancy in the ablation rates at the very surface of ECD Sn and Cu layers was attributed to surface roughness, which, however, tends to level out with increasing depth of the crater.²² In this respect, the Cu surface roughening by the antecedent ablation of the Sn upper layer could help the ablation of the Cu lower layer. Other theories involving stress-induced defect formation in the lower lying layers upon phase explosion could be an alternative explanation for this phenomenon. In fact the reduction of the damage threshold was found to correlate with

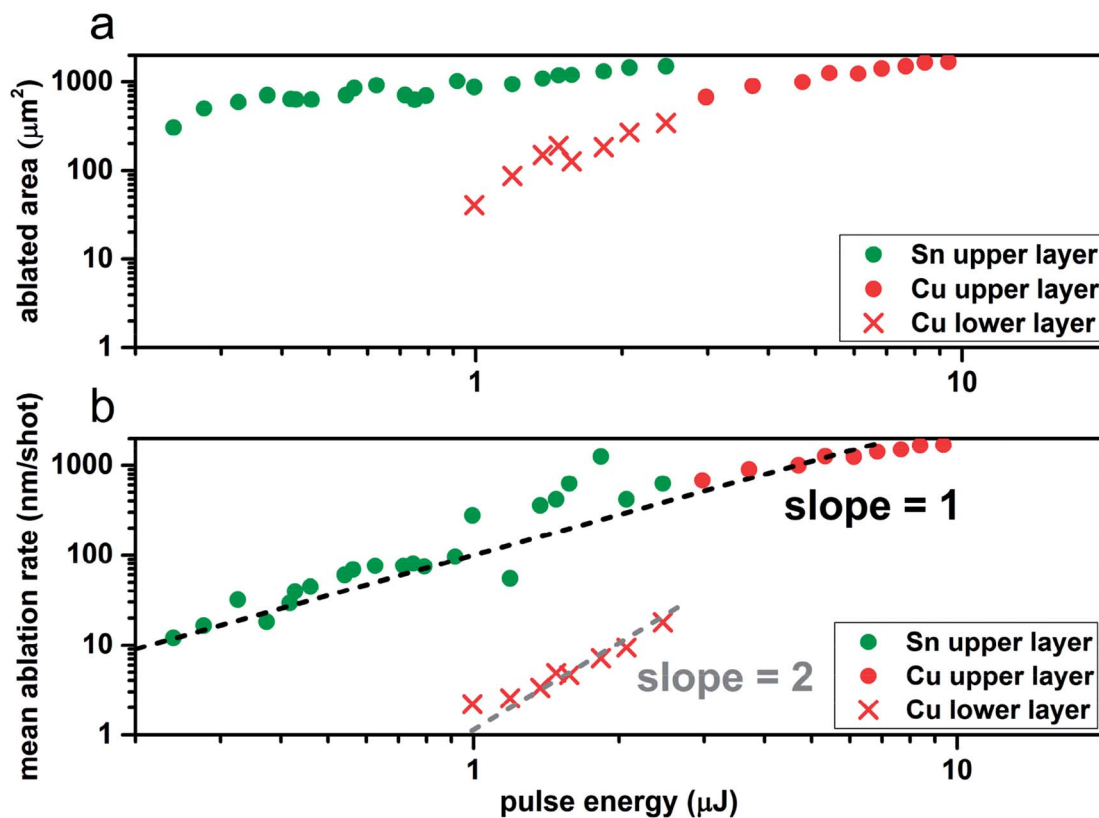


Fig. 7 Dependence of (a) the ablated area and (b) the mean ablation rate on the laser pulse energy in a range of 0.2–9.4 μJ. Each data point represents the mean of three experimental repeats with 500 applied single laser shots.

the number of applied laser shots.⁴³ It is known that after the event of phase explosion, which occurs upon intense femto-second laser irradiation of solids and their heating above the critical temperature,⁴⁴ adiabatic cooling and thermal expansion may result in an intense thermoelastic wave.⁴⁵ The increased Cu ablation when Cu appears in the lower layer might be the result of the occurrence of such a thermoelastic wave formed in the Sn layer already at lower energies that penetrates into the Cu layer causing spalling or fragmenting^{46,47} and expulsion of the material.

Another possible explanation could be related to the time-scale of the system's response to the laser irradiation. Laser ablation is accompanied by free electron generation above the surface and takes place in the time range of approximately 10^{-13} s, thus following the temporal profile of the laser down to the fs-range.⁴⁸

Given that Sn is a much worse electrical conductor than Cu the generated free electrons could accumulate in the plume volume forming an electron cloud above the surface that within this time scale acts as an electron shield absorbing the laser flux, reducing thereby the ablation efficiency of the Cu material. Data points coming from the lower layer Sn in sample type 2 are missing in Fig. 7, because under the harsh conditions needed to efficiently ablate the upper Cu layer, the lower Sn layer was ablated after applying only a very few laser shots. The calculation of the mean ablation rate under such circumstances would then result in a big uncertainty of such data points and hardly

allow for any chemical quantitative statement. A solution to the problem could be achieved by a two-step ablation process: by online-monitoring of the signal on the measurement computer the analysis could be stopped at the interface and the laser power could be reduced before entering the Sn phase. In the first stage the Cu deposit would need to be ablated by using the lowest possible laser irradiance until an abrupt decrease of the Cu signal going along with the simultaneous rise of the Sn intensity would be observed. The laser irradiation would then temporarily be stopped and subsequently be resumed after setting the laser conditions just above the ablation threshold of Sn. This strategy was already proved to be successful for multi-layered samples containing organic phases.¹⁹ However, as the target sample of this study does not contain Sn underneath Cu, this strategy was not employed and the ablation rate for Sn in this constellation was not further investigated.

Depth profiling approaches with reduced side-wall contributions

The pronounced differences in the ablation conditions of Sn and Cu, which have been discussed in the previous paragraphs, prohibit chemical depth profiling of their double layer systems that cannot be achieved with a single parameter set for laser ablation. If the laser pulse energy is chosen high enough, like *e.g.* 2.5 μJ as used for the single-step approach in this particular study, it is in principle possible to drill through Sn, Cu, and even

the underlying Si substrate with a single set of conditions. However the resulting depth profile analysis will not provide sufficiently high depth resolution. Also the mass spectra recorded under such conditions will suffer from low mass resolution due to the occurrence of surface and space charge effects, which can significantly perturb the ion trajectories in the instrument. The Sn layer will likely be ablated in 1 or 2 shots, which makes it impossible to obtain any detailed chemical depth information on it. Additionally, there will be a large degree of side-wall contributions from the upper layer influencing the quality of the depth profile. We therefore recommend to use a multi-step approach for depth profiling instead, which reduces the extent of the mentioned drawbacks of using only one set of parameters, here mainly applied pulse energy.

In the following, we will investigate two multi-step approaches of patterned ablation schemes, denoted as ‘flower’ and ‘rectangular’ approaches according to the particular geometrical raster shot scheme used in the intermediate surface preparation step. Fig. 8a shows the initially mentioned single-step approach and compares this one to the other two approaches, whose geometrical shot schemes are given at the right hand side of Fig. 8b and c. The EDX maps presented in this figure indicate that all three approaches are suitable to ablate Sn and Cu efficiently and to reach the Si substrate. The

normalized depth profiles obtained from these three experiments are shown in Fig. 9a–c. In the case of the single-step approach (Fig. 9a), sufficiently high laser pulse energy was used to obtain the depth profile of both layers in one measurement. However, for this pulse energy the entire 2.5 μm thick Sn layer was ablated within a few laser shots, which resulted in a poor depth resolution. Moreover, the Sn signal remained noticeable throughout the whole depth profile measurement due to a high degree of side-wall contributions.

In the case of the ‘rectangular’ approach (Fig. 9b), the pulse energy was separately optimized for both the Sn and the Cu layer to allow the individual depth profiling with sufficiently high depth resolution. In the first step, a depth profile of the Sn layer was measured. After doing so, the surface around the Sn crater was submitted to an extra surface cleaning treatment by applying the same number of shots and the same laser pulse energy as for the depth profile measurement repeatedly in the shape of a ‘rectangular’-like structure (see Fig. 8b, right panel). Then the laser pulse energy was changed and the depth profile of the Cu layer was measured at the initial Sn crater site. After an area of Cu as the base signal with only minor Sn contributions, the Si layer is reached and clearly penetrated (data not shown in Fig. 9).

The ‘flower’ approach (Fig. 9c) was conducted in a similar three-step procedure as described for the ‘rectangular’ approach only with a different 2D geometry of surface preparation step 2 (Fig. 8c, right panel). Here, the Sn depth profile obtained in step 1 is more expanded, because a slightly lower laser pulse energy was applied compared to the ‘rectangular’ approach.

With the conditions used in this approach, only very little Si was ablated from the Si substrate layer underneath the ECD metal films by the applied 500 single laser shots. Nevertheless, the onset of the Si signal is clearly visible.

In depth profiling studies of multilayer samples using (fs-) LI-TOFMS^{49–51} the averaged ablation rate (AAR) is defined as the number of laser shots necessary until the measured intensity of the first layer (here Sn) drops to 50% of the maximum intensity (P_{50}). The region between P_{50} of Sn and P_{50} of Cu is considered as the interface region.

In this report, we investigate the contribution of the Sn signal emerging from the side walls while profiling the Cu layer. Here we compare two cases: (i) the Sn fraction in the accumulation of the Cu and Sn signal starting from the first detection of Cu until the first detection of Si, and (ii) the Sn fraction in the accumulation of the Cu and Sn signal starting from P_{50} of Cu until the first detection of Si. The side-wall contributions obtained for these two cases are presented in Fig. 10 as red and green columns (cases (i) and (ii), respectively). The analysis of the certified reference material BCS-CRM 374 (BAS Ltd., UK) indicated that the Sn signal was overestimated with respect to the Cu signal detected in our experiments by a factor of up to 2 depending on the applied laser pulse energy. This uncertainty is accounted for by the error bars in Fig. 10.

As expected, the highest fraction of side-wall contributions was observed for the single-step approach. This observation holds true for both considered cases, as a significant

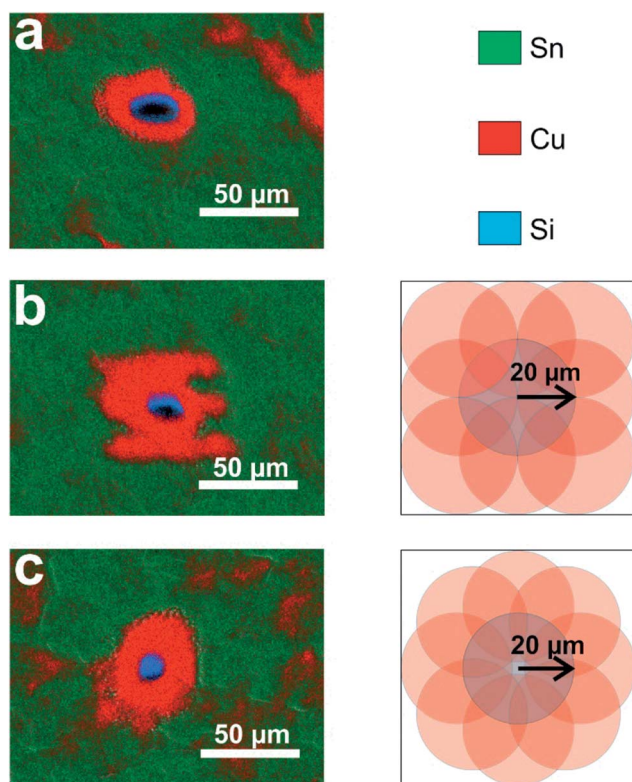


Fig. 8 EDX maps and laser shot schemes of different depth profiling approaches. (a) Single-step approach, (b) ‘rectangular’ approach, and (c) ‘flower’ approach. EDX maps show Sn (green), Cu (red), and Si (blue). The laser shot schemes illustrate the distribution and the approximate size of the laser-induced craters in Sn and Cu formed at the applied laser pulse energy.

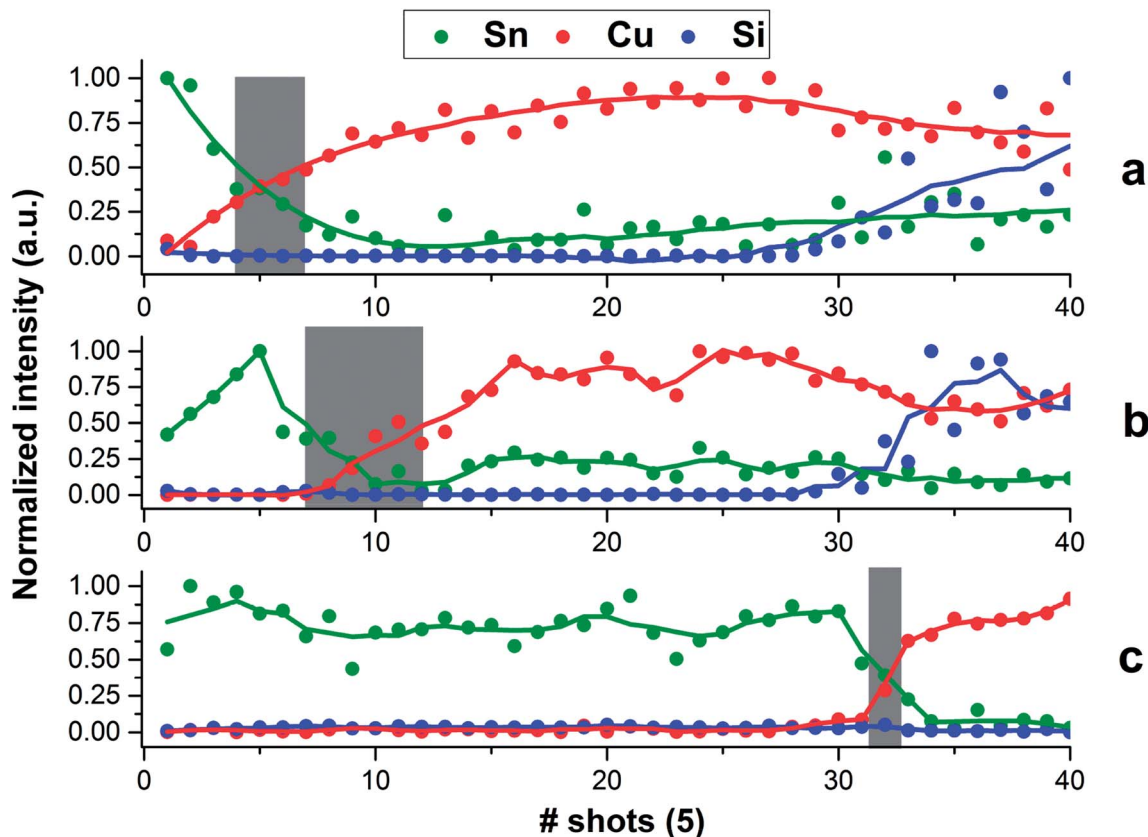


Fig. 9 Depth profiles obtained from the different depth profiling approaches presented in Fig. 8: (a) single-step approach, (b) 'rectangular' approach, and (c) 'flower' approach. The plotted intensity for each element has been normalized to its respective highest intensity value. The profiles are given with the following colour code: Sn = green, Cu = red, and Si = blue. All profiles are obtained from averaging 5 laser shots to one data point each. The grey vertical bars indicate the interface region between the Sn and the Cu layer. The solid lines are given to guide the eye.

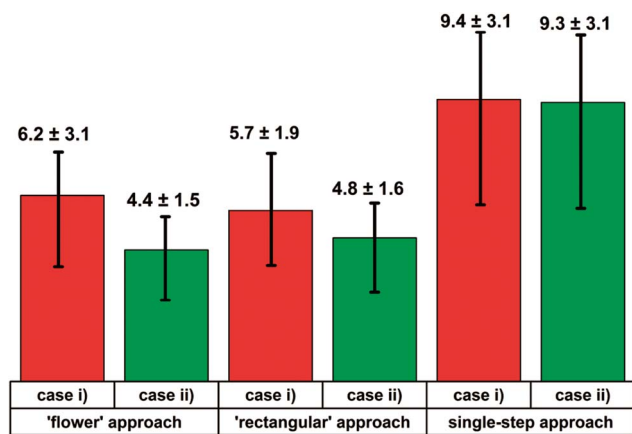


Fig. 10 Fraction of side-wall contributions for different depth profiling approaches. The red and green columns represent the results obtained for cases (i) and (ii), respectively.

contribution of the Sn material close to the main crater walls results in a constant surface Sn signal that adds to the Cu depth profile and disturbs the latter. The two three-step processes, the 'flower' and the 'rectangular' approach, show significantly fewer side-wall contributions. However, the perfect positioning of the

individual craters in the shot masks is not trivial in the current experimental setup due to limited accuracy ($\pm 3\text{--}5\ \mu\text{m}$) in the positioning of the translation stages. Furthermore, the measurements show that Sn originating from the uppermost surface layer can still be detected within the Cu layer. This is most likely due to contribution from the beam wings which result in the formation of a pronounced affected zone on the Sn layer when applying high laser pulse energy for the ablation of the Cu layer in the second analysis step.

The quality of the individual depth profiling approaches can be assessed based on the determination of both the degree of side-wall contributions and the AAR. Note that the lower the AAR value, the higher the degree of obtainable depth information of the investigated layers. The AAR values for Sn in the single-step approach, the 'rectangular' and the 'flower' approach are $0.13\ \mu\text{m}$ per pulse, $0.07\ \mu\text{m}$ per pulse and $0.02\ \mu\text{m}$ per pulse, respectively. Therefore, the 'flower' approach can be considered as the most promising to obtain well-resolved depth profiles of Sn and Cu with minimized side-wall contributions, while the single-step approach is clearly the least suitable procedure.

As discussed in the previous sections, much less pulse energy is needed to ablate Sn than to ablate Cu. Therefore, also the laser pulse wings may be intense enough to induce the

ablation of Sn while profiling Cu. When looking at Fig. 8b it becomes clear that a signal from the Sn protrusions formed after the reflow of the material on both sides of the raster boundaries will necessarily contribute to the Cu depth profile. This becomes evident from the sharp drop of the Sn signal in the depth profile shown in Fig. 9b. For further reduction of side-wall contributions, an intermediate surface-cleaning step should consequently be performed in terms of a much larger raster to avoid the undesired layer intermixing. However, the fact that the surface preparation in the second step of the measurement procedure leaves the Cu surface at least largely 'pre-cleaned' from Sn allows obtaining a significantly improved Cu depth profile in step 3, in both considered cases.

Conclusions

Continuously striving for the miniaturization of unit structures concomitant with the gain of performance in the semiconductor industry gives rise to smaller-sized, yet more complex IC architectures, which in turn indicates the necessity of improved solder technology, like *e.g.* recently developed binary Sn–Cu solder bumps. To date, these highly sophisticated and technologically demanding systems lack an appropriate analytical technique for quantitative depth chemical analysis. fs-LI-TOFMS is a state-of-the-art approach to close this analytical accessibility gap. However, detailed knowledge on the specific requirements these systems pose has only recently emerged and much work remains to be done in this field.

For the first time, we report a dedicated study on the quantification of side-wall contributions in the course of fs-laser ablation mass spectrometry depth profiling experiments using the LMS instrument. The choice of bi-layer Sn–Cu test systems allows us to gain insights into this phenomenon that is difficult to study in homogeneous systems. Furthermore, these layered samples closely resemble industrially manufactured Sn–Cu solder bumps, which are of significant technological interest. In particular, obtaining their depth profiles to quantify and locate possible organic contaminants is a high-priority goal. With the investigations reported here, we have identified the pre-requisites for chemical quantitative depth profile measurements of multi-layer metal–semiconductor systems similar to these Sn–Cu solder bumps and we have compared different general approaches to experimentally tackle the task. Based on these proof-of-concept measurements, we conclude that the best approach for obtaining chemical quantitative depth profile measurements of these highly diverse and demanding systems is a three-step process composed of two analysis and one intermediate surface preparation steps. In the first analysis step, the upper layer material is profiled under optimized conditions. The second step is the surface pre-treatment step, where the upper layer material in an area around the crater resulting from step 1 is removed. This results in a directly accessible lower layer surface, which is analysed in step three with optimized parameters.

It turns out that surface pre-treatment step 2 is the most crucial for the success of this method. It should be conducted in a laterally expanded, raster-like fashion with a high degree of

overlap between individual craters. As we have shown, this allows reducing side-wall contributions.

To further improve the results, the laser pulse energy used to generate the depth profile of the Sn layer should be reduced to yield a higher depth resolution. The laser pulse energy used to ablate the Sn and the extent of crater overlap in the pre-cleaning step should be optimized with regard to complete Sn ablation. The lateral expansion of the raster should be increased further to avoid interaction of the beam wings with the affected zone of the upper Sn layer. Knowing the fraction of side-wall contributions resulting from such an improved experiment, the lower layer depth profile can be corrected to obtain a representative depth profile. Combining the two individual profiles then yields the entire profile of the system. This analysis approach will be applicable not only to the as-prepared Sn solder bumps on Cu pillars, but with slight adjustments also to the reflowed system.

Conflicts of interest

There are no conflicts to declare.

Acknowledgements

This work is supported by the Swiss National Science Foundation. Furthermore, it was performed with the support of the interfaculty Microscopy Imaging Centre (MIC) of the University of Bern. We gratefully acknowledge the wafer supply by imec.

Notes and references

- 1 S. W. Jung, J. P. Jung and Y. Zhou, *IEEE Trans. Electron. Packag. Manuf.*, 2006, **29**, 10–16.
- 2 D. Li, C. Liu and P. P. Conway, *Mater. Sci. Eng., Proc. Conf.*, 2005, **391**, 95–103.
- 3 Y. Liu, J. Wang, L. Yin, P. Kondos, C. Parks, P. Borgesen, D. W. Henderson, E. J. Cotts and N. Dimitrov, *J. Appl. Electrochem.*, 2008, **38**, 1695–1705.
- 4 R. S. Rai and S. Subramanian, *Prog. Cryst. Growth Charact. Mater.*, 2009, **55**, 63–97.
- 5 F. Reniers and C. Tewell, *J. Electron Spectrosc. Relat. Phenom.*, 2005, **142**, 1–25.
- 6 J. S. Becker, in *Inorganic Mass Spectrometry*, John Wiley & Sons, Ltd, 2007, DOI: 10.1002/9780470517222.fmatter.
- 7 J. S. Becker, in *Inorganic Mass Spectrometry*, John Wiley & Sons, Ltd, 2007, pp. 1–6, DOI: 10.1002/9780470517222.ch.
- 8 R. Escobar Galindo, R. Gago, D. Duday and C. Palacio, *Anal. Bioanal. Chem.*, 2010, **396**, 2725–2740.
- 9 G. Qian, Y. Li and A. R. Gerson, *Surf. Sci. Rep.*, 2015, **70**, 86–133.
- 10 A. Cerezo, P. H. Clifton, M. J. Galtrey, C. J. Humphreys, T. F. Kelly, D. J. Larson, S. Lozano-Perez, E. A. Marquis, R. A. Oliver, G. Sha, K. Thompson, M. Zandbergen and R. L. Alvis, *Mater. Today*, 2007, **10**, 36–42.
- 11 E. W. Bohannon, L.-Y. Huang, F. S. Miller, M. G. Shumsky and J. A. Switzer, *Langmuir*, 1999, **15**, 813–818.

- 12 J. C. Vickerman and N. Winograd, *Int. J. Mass Spectrom.*, 2015, **377**, 568–579.
- 13 N. T. M. Hai, D. Lechner, F. Stricker, J. Furrer and P. Broekmann, *ChemElectroChem*, 2015, **2**, 664–671.
- 14 B. Fernández, R. Pereiro and A. Sanz-Medel, *Anal. Chim. Acta*, 2010, **679**, 7–16.
- 15 A. Gutierrez-Gonzalez, C. Gonzalez-Gago, J. Pisonero, N. Tibbetts, A. Menendez, M. Velez and N. Bordel, *J. Anal. At. Spectrom.*, 2015, **30**, 191–197.
- 16 S. J. M. Van Malderen, J. T. van Elteren and F. Vanhaecke, *Anal. Chem.*, 2015, **87**, 6125–6132.
- 17 N. T. M. Hai, J. Odermatt, V. Grimaudo, K. W. Krämer, A. Fluegel, M. Arnold, D. Mayer and P. Broekmann, *J. Phys. Chem. C*, 2012, **116**, 6913–6924.
- 18 V. Grimaudo, P. Moreno-García, A. Riedo, M. B. Neuland, M. Tulej, P. Broekmann and P. Wurz, *Anal. Chem.*, 2015, **87**, 2037–2041.
- 19 P. Moreno-García, V. Grimaudo, A. Riedo, M. Tulej, M. B. Neuland, P. Wurz and P. Broekmann, *Electrochim. Acta*, 2016, **199**, 394–402.
- 20 P. Moreno-García, V. Grimaudo, A. Riedo, M. Tulej, P. Wurz and P. Broekmann, *Rapid Commun. Mass Spectrom.*, 2016, **30**, 1031–1036.
- 21 A. Riedo, A. Bieler, M. Neuland, M. Tulej and P. Wurz, *J. Mass Spectrom.*, 2013, **48**, 1–15.
- 22 V. Grimaudo, P. Moreno-García, A. Riedo, S. Meyer, M. Tulej, M. B. Neuland, M. Mohos, C. Gutz, S. R. Waldvogel, P. Wurz and P. Broekmann, *Anal. Chem.*, 2017, **89**, 1632–1641.
- 23 U. Rohner, J. A. Whitby and P. Wurz, *Meas. Sci. Technol.*, 2003, **14**, 2159.
- 24 A. Riedo, M. Neuland, S. Meyer, M. Tulej and P. Wurz, *J. Anal. At. Spectrom.*, 2013, **28**, 1256–1269.
- 25 M. B. Neuland, S. Meyer, K. Mezger, A. Riedo, M. Tulej and P. Wurz, *Planet. Space Sci.*, 2014, **101**, 196–209.
- 26 M. Tulej, M. Iakovleva, I. Leya and P. Wurz, *Anal. Bioanal. Chem.*, 2011, **399**, 2185–2200.
- 27 A. Riedo, S. Meyer, B. Heredia, M. B. Neuland, A. Bieler, M. Tulej, I. Leya, M. Iakovleva, K. Mezger and P. Wurz, *Planet. Space Sci.*, 2013, **87**, 1–13.
- 28 S. Meyer, A. Riedo, M. B. Neuland, M. Tulej and P. Wurz, *J. Mass Spectrom.*, 2017, **52**, 580–590.
- 29 J. Bonse, J. Krüger, S. Höhm and A. Rosenfeld, *J. Laser Appl.*, 2012, **24**, 042006.
- 30 G. H. Aylward and T. J. V. Findlay, *Datensammlung Chemie in SI-Einheiten*, 1999.
- 31 J. M. Vadillo, C. C. Garcia, J. F. Alcantara and J. J. Laserna, *Spectrochim. Acta, Part B*, 2005, **60**, 948–954.
- 32 A. Borowiec and H. K. Haugen, *Appl. Phys. Lett.*, 2003, **82**, 4462–4464.
- 33 A. Y. Vorobyev, V. S. Makin and C. Guo, *J. Appl. Phys.*, 2007, **101**, 034903.
- 34 J. Bonse, H. Sturm, D. Schmidt and W. Kautek, *Appl. Phys. A: Mater. Sci. Process.*, 2000, **71**, 657–665.
- 35 J. E. Sipe, J. F. Young, J. S. Preston and H. M. van Driel, *Phys. Rev. B: Condens. Matter Mater. Phys.*, 1983, **27**, 1141–1154.
- 36 J. Bonse, M. Munz and H. Sturm, *J. Appl. Phys.*, 2005, **97**, 013538.
- 37 J. Bonse, A. Rosenfeld and J. Krüger, *J. Appl. Phys.*, 2009, **106**, 104910.
- 38 M. López-Claros, J. M. Vadillo and J. J. Laserna, *J. Anal. At. Spectrom.*, 2015, **30**, 1730.
- 39 J. F. Alcántara, J. M. Vadillo and J. J. Laserna, *J. Anal. At. Spectrom.*, 2010, **25**, 1424–1431.
- 40 K.-W. Moon, W. J. Boettinger, U. R. Kattner, F. S. Biancanello and C. A. Handwerker, *J. Electron. Mater.*, 2000, **29**, 1122–1136.
- 41 K. S. Kim, S. H. Huh and K. Suganuma, *J. Alloys Compd.*, 2003, **352**, 226–236.
- 42 A. Zribi, A. Clark, L. Zavalij, P. Borgesen and E. J. Cotts, *J. Electron. Mater.*, 2001, **30**, 1157–1164.
- 43 X. Ni, C.-y. Wang, L. Yang, J. Li, L. Chai, W. Jia, R. Zhang and Z. Zhang, *Appl. Surf. Sci.*, 2006, **253**, 1616–1619.
- 44 P. Lorazo, L. J. Lewis and M. Meunier, *Phys. Rev. Lett.*, 2003, **91**, 225502.
- 45 N. Zhang, X. Zhu, J. Yang, X. Wang and M. Wang, *Phys. Rev. Lett.*, 2007, **99**, 167602.
- 46 L. V. Zhigilei and B. J. Garrison, *J. Appl. Phys.*, 2000, **88**, 1281–1298.
- 47 D. Perez and L. J. Lewis, *Phys. Rev. Lett.*, 2002, **89**, 255504.
- 48 B. Rethfeld, K. Sokolowski-Tinten, D. von der Linde and S. I. Anisimov, *Appl. Phys. A: Mater. Sci. Process.*, 2004, **79**, 767–769.
- 49 C. Garcia, J. Vadillo, S. Palanco, J. Ruiz and J. Laserna, *Spectrochim. Acta, Part B*, 2001, **56**, 923–931.
- 50 C. C. Garcia, J. M. Vadillo, J. Ruiz and J. J. Laserna, *J. Anal. At. Spectrom.*, 2003, **18**, 779–782.
- 51 M. He, B. Li, S. Yu, B. Zhang, Z. Liu, W. Hang and B. Huang, *J. Anal. At. Spectrom.*, 2013, **28**, 499–504.